16

Sintering and Characterization of Rare Earth Doped Bismuth Titanate Ceramics Prepared by Soft Combustion Synthesis

Umar Al-Amani Azlan, Warapong Krengvirat, Ahmad Fauzi Mohd Noor, Khairunisak Abd. Razak and Srimala Sreekantan
Universiti Sains Malaysia, USM, Pulau Pinang
Malaysia

1. Introduction

Nowadays, ferroelectric ceramics and thin films have attracted much attention for various studies which are generally used for numerous potential applications in ferroelectric random access memory (FRAM), in microelectronic mechanical system (MEMS), non-linear optical devices, surface acoustic wave devices, tunable capacitors, sensing applications or pyroelectric detectors (Besland et al., 2006, Yang et al., 2008). The main focus to develop the ferroelectric thin films has started in 1980s (Besland et al., 2006). Several methods were initially used for deposition of thin films such as conventional dipping, sputtering and spin coating techniques. Typically, the deposition of thin films will be more complex to obtain a good layer that consists of several ferroelectric compounds on substrate. Furthermore, high precision deposition technique is essential to control the desired thickness and surface layer of ferroelectric compounds. As far as our concern, the up to date technique such as physical vapor deposition (PVD), RF sputtering, chemical vapor deposition (CVD) and metal-organic chemical vapor deposition have been frequently used in many studies to obtain a better ferroelectric thin films condition. Nevertheless, a major concern on expensive equipment and experience user limit this technique in many studies. In order to develop the ferroelectric materials, the preparation in the form of bulk ceramics has been extensively studied. Up to now, several methods, including solid state reaction, hydrothermal synthesis, mechanical activation technique, sol-gel method, co-precipitation method were used for the preparation of bulk ceramics. Recently, the soft combustion synthesis is used as alternative route since it offers several beneficial points to the processing element and the properties of ceramics (Yan ,Razak, 2010). Bismuth titanate, $Bi_4Ti_3O_{12}$ or BTO has received a lot of attention as dielectric and ferroelectric materials. Many studies have been conducted in various processing route to improve the microstructure that has a significance effect on dielectric and ferroelectric properties (Hardy et al., 2004, Pookmanee et al., 2004, Zhi-hui et al., 2010). In addition, a modification on basic compound is essential to enhance those properties. Since BTO is also sought as a potential material for dielectric application, in this chapter the effect of Sm^{3+} and Pr^{3+} doped-BTO was prepared and characterized by soft combustion technique. In order to investigate a possible application as wireless dielectric antenna, the dielectric study at different frequencies was carried out.

2. Bismuth titanate and other properties

Considerable attention has recently been paid to bismuth layer-structured ferroelectric (BLSF) as ferroelectric materials instead of unfriendly lead (Pb)-based ferroelectrics because of its excellent fatigue resistance and Pb-free chemical composition (AlguerÃ³ et al., 2006, Subbarao, 1961, Xue et al., 2009, Yang et al., 2003). The general formula is given by $(Bi_2O_2)^{2+}$ $(A_{m-1}B_mO_{3m-1})^{2-}$ where A = Bi^{3+}, Pb^{2+} Sr^{2+}, Ba^{2+}, etc. and B = Nb^{5+}, Ta^{5+}, Ti^{4+}, etc. m = 1, 2, 3, 4, 5, etc. $(Bi_2O_2)^{2+}$ is the bismuth oxide layer and $(A_{m-1}B_mO_{3m+1})^{2-}$ is the pseudo perovskite layer (Armstrong ,Newnham, 1972, Newnham et al., 1971, Yan et al., 2006). BLSF is expected to have various numbers of pseudo perovskite blocks in unit cells. BLSF, bismuth titanate, $Bi_4Ti_3O_{12}$ (m = 3) or BTO has three pseudo perovskite blocks in half-unit cells. In simple words, its structure can be described as formed by three unit cells of $(Bi_2Ti_3O_{10})^{2-}$ with perovskite like structure interleaved with $(Bi_2O_2)^{2+}$ layers (Ng et al., 2002). BTO is an attractive material that has low processing temperature (700-750^{o}C) than other BLSF (e.g. $SrBi_2Ta_2O_9$) and strong anisotropy of the spontaneous polarization (P_s) along the *a*-axis (~ 50 μC/cm^2) and *c*-axis (~ 4 μC/cm^2) (Wang et al., 1999, Zhi-hui et al., 2010). However, the low remanent polarization (P_r = 5 μC/cm^2), low fatigue resistance and high dielectric loss of BTO would limits its application in FRAM applications. The reduction in remanent polarization and fatigue with high dielectric losses become more serious issues due to defects in perovskite structure whereby the Bi ions volatile during sintering process and create the Bi vacancies accompanied by oxygen vacancies. Nevertheless, there are advantages on BTO whereby it has high Curie temperature at 675^{o}C and high dielectric permittivity (~ 200), making this material for other possible applications such as capacitors, antennas, sensors and piezoelectric (Golda et al., 2011).

3. Rare-earth doping and other properties

Recent studies revealed that ion substitution in perovskite BTO structure is an efficient technique for improving the drawbacks of BTO as ferroelectric ceramics (Cui ,Hu, 2009, Santos et al., 2009, SimÃµes et al., 2008). It was reported that the fatigue free films with excellent ferroelectric properties are obtained by substitution of Bi-site ions in BTO films for La^{3+} ions using a pulsed laser deposition (Park et al., 1999). This ion substitution resulted in large remanent polarization value over 20μC/cm^2, which was considerably higher than that of BTO films. Furthermore, it has good fatigue resistance, low leakage current at 10^{-7} A/cm^2 at 5V and low processing temperature approximately in the range of 650 to 700^{o}C. Recently, it has been reported that the substitution of Nd^{3+} in BTO thin films was more effective for improving the ferroelectric properties than La substitution (Kim ,Kim, 2005). This result can be explained by the fact that the substitution of Bi^{3+} by rare-earth ions with a smaller ionic radius for the Bi^{3+} site is effective in improving the ferroelectric properties. In this case, the ionic radius of Nd^{3+} is much smaller than those of Bi^{3+} and La^{3+}. According to both studies, it is necessary to find out more rare-earth elements with smaller ionic radius in other to enhance the ferroelectric properties of BTO ceramics. Besides that, a small amount of rare-earth elements is important to tailor the microstructures of BTO. Recently, it was reported that Nd doping into BTO ceramics act as a grain-growth inhibitor whereby a remarkable decrease in the grain size with fine and homogeneous microstructure (Kan et al., 2008). It is well known that typical BTO powders

are attributed to high anisotropic grains, in which the ferroelectric properties are grain orientation dependent. Thus, it can be said that the homogeneity in microstructure is strongly influenced by rare-earth content. In addition, the corresponding microstructure can produce better ferroelectric properties. The summary of doping studies in BTO and their properties are listed in **Table 1**. Based on this summary, the selection of processing route is important to determine the grain orientation and microstructure as well as dielectric and ferroelectric properties. Besides that, the doping studies can improve the dielectric and ferroelectric properties of BTO.

Rare-earth	Process	XRD	Microstructure	Dopant content	ε_r	tan δ	P_r	E_c
La^{3+} (47)	Polymeric precursor method			0 0.25 0.5 0.75	86 104 112 148 at 1 MHz	0.008 0.0011 0.0068 0.0018	15.1 20.2 20.2 20.3	1.45 1.09 0.66 0.99
La^{3+} (38)	Sol-gel	Randomly oriented at 700°C for 30 minute		0 0.85			12.5 18.6	2.8 2.8
La^{3+} (18)	Conventional solid state reaction			0 0.5 0.75 1 1.5 2	130 145 147 186 168 101 at 100 kHz	0.022 0.023 0.024 0.022 0.017 0.014		
Nd^{3+} (50)	Pulsed laser deposition	Highly *c*-axis oriented		0 0.85	103 177 at 500 kHz	0.063 0.068	4.5 8.6	142 88
Nd^{3+} (24)	Solid state reaction			0.75 0.80 0.85 0.90	174 143 158 179	0.0603 0.0055 0.0044 0.0070	11.1	
Nd^{3+} (52)	Solid state reaction		Plate-like grains	0 0.25 0.5 0.75 1	108 128 132 148 160	0.0078 0.0045 0.0044 0.0040 0.0039	5.2 5.5 9.3 11.1 9.8	27 35.2 45.2 42 34
Nd^{3+} (53)	Metal organic solution decomposition	Highly *c*-axis oriented grains	Plate-like grains	0.5 0.75	172 156		17 19	150 98
Sm^{3+} (56)	Solid state reaction	Randomly oriented	Plate-like grains	0.8	270	0.003	16	70

Table 1. Summary of doping studies in BTO and their properties.

4. Processing route for preparation the BTO and rare-earth doping

As is known, synthesis process plays a crucial role to determine the microstructure of the ceramics as well as the control purity and stoichiometry. Different synthesis methods have been developed for the production of perovskite powders, like solid state reaction, sol-gel technique, hydrothermal synthesis, co-precipitation and combustion synthesis (Hardy et al., 2004, Kim, 2006, Kojima et al., 2009, Macedo et al., 2004, Pookmanee ,Phanichphant, 2009). It was reported that the ferroelectric properties of BTO can also be improved with a specific control in terms of microstructure, chemical homogeneity and its purity (Lu et al., 2005, Yang et al., 2008). Nevertheless, there are several merits and drawbacks of each synthesis process in order to control the ferroelectric domains through the preferred microstructure as well as crystal structure. Thus, the description of each synthesis process is discussed in the following subsection.

4.1 Conventional solid state reaction

The conventional solid state reaction is mostly used for preparation of bulk ceramics. It is an endothermic reaction used to produce simple oxide from carbonates, hydroxides and other metal salts. Such conventional reaction often results in high agglomeration and compositional inhomogeneity of powders because of high calcination temperature and repeated grinding. As a result, the sinterability of ceramics is fairly low subsequently a higher sintering temperature is required to enhance their properties. Subbarao (Subbarao, 1961, Subbarao, 1962) prepared the BTO ceramics using the solid state reaction and sintered from 1000 to 1250^{o}C to achieve the theoretical density of about 80 %. In some cases, the sintering condition with longer soaking time is needed to enhance other properties. Watcharapasorn et al. (Watcharapasorn et al., 2010) studied the grain growth behavior of BTO ceramics using different sintering conditions. It was reported that the sintering of ceramics for longer time could render a material with more isotropic microstructure with reduced preferred orientation. Nevertheless, the increase in relative density (91 – 94 %) was very small with increasing soaking time.

4.2 Mechanical activation technique

Mechanical activation technique was initially derived from mechanical alloying for synthesizing alloys and intermetallics. The corresponding technique is a common part of the powder preparation route in the field of ceramics where high-energy ball milling has become a conventional method for producing nanocrystalline materials. This technique uses low-cost and widely available oxides as starting materials and skips the calcination step at an intermediate temperature, leading to a simplified process (StojanoviÄ‡ et al., 2008). Furthermore, the mechanically derived powders have higher sinterability than those powders synthesized by the conventional ball milling. Kong et al. (Kong et al., 2001) obtained the large P_r (24 μC/cm^2) and low E_c (11 kV/cm) for BTO ceramics with better density of 98 % after low temperature sintering at 850^{o}C for the powder derived from mechanical activation technique. Stojanovic et al. (Stojanovic et al., 2006, Stojanovic et al., 2006) reported that the BTO powder can be directly synthesized using high impact milling for about 3 to 12 hours and then sintered at 1000^{o}C for 2 h. Han et al. (Han ,Ko, 2009) stated the formation of BTO phase is highly dependent on the processing parameters particularly

the impact energy or milling intensity. Zdujic et al. (ZdujiÄ‡ et al., 2006) reported that a mixture of α-Bi_2O_3 transformed to $Bi_2O_2CO_3$ at a milling intensity of ~ 0.49 W/g, which in turn was converted directly into a nanocrystalline BTO phase when the intensity was increased to ~ 2.68 W/g. Thus, it can be concluded that the parameter of mechanical milling has a significance result on the particle morphology and sinterability.

4.3 Sol-gel synthesis

The most popular wet chemical technique like sol-gel synthesis is widely used since it offers excellent uniformity over a large area, easy composition control, short fabrication time, as well as a low temperature process at comparatively a low cost (Du et al., 2007). This technique can be used to prepare the samples in the form of bulk ceramics and thin films. Several factors that need to be considered in a sol-gel synthesis are solvent, precursors, catalyst, pH, additives and mechanical agitation (Du et al., 2007, Guo et al., 2007, Ke et al., 2010). These factors greatly influence the powder size and other properties. Du et al. (Du et al., 2007, Du et al., 2008) reported that a highly stable and homogeneous BTO powders was produced at calcination temperature as low as 550^{o}C, which is fairly low in wet chemical technique.

4.4 Hydrothermal synthesis

Another wet chemical technique is known as hydrothermal synthesis. In hydrothermal synthesis, the reaction mixture is heated above the boiling point of water in an autoclave or other closed system and the sample is exposed to steam at high pressures (Pookmanee et al., 2004, Shi et al., 2000, Yang et al., 2003). In addition, the parameter of Teflon-lined vessel such as temperature and reaction time are mainly important factor to determine the phase structure and particle morphology (Pookmanee et al., 2004). It was also reported that the hydrothermally powder was significantly influenced by different mineralizer KOH content and molar ratio of Bi/Ti (Shi et al., 2000). Recently, Xie et al. (Xie et al., 2007) reported that the concentration of KOH, reaction time and temperature had a significant effect on the phase composition and morphology of the resultant single crystals. Many authors reported that hydrothermal synthesis has several advantages including narrow particle size distribution, highly purity with fine powder, and low degree of agglomeration. In processing stand point, the hydrothermal synthesis is able to synthesize powder at a much lower temperature compared to other methods. Nevertheless, the synthesis in an aqueous environment causes water to be incorporated into the powder, thus causing deterioration in the electrical properties (Yan ,Razak, 2010).

4.5 Co-precipitation method

In order to prepare the controlled morphology, narrow particle size distribution, high purity and high degree of crystallinity as well as possible reduction in sintering temperature, the co-precipitation method might be a promising route instead of other wet chemical route. Precipitation is the formation of a solid product or powder from a liquid solution which initiated by either changing the solution temperature, pressure, pH or using a chemical precipitation agent so as to exceed the solubility limit of the desired species (Pookmanee, Phanichphant, 2009, Thongtem ,Thongtem, 2004). In general, co-precipitation reaction relies

on dissolving the metal salts, commonly metal chlorides, nitrates and hydroxides followed by a rapid pH change to form precipitate. The precipitate must be thoroughly washed to get rid of the impurities from the solutions prior to calcination. It was reported that the well-dispersed particles of about 10 nm began to form a BTO phase at 470^{o}C. The phase formation was complete after a 550^{o}C for 30 minute heat treatment. It was finally sintered at 750^{o}C for 1 hour to achieve a sample of high density of 97.2% (Kan et al., 2002).

4.6 Soft combustion synthesis

The synthesis of BTO powders using combustion reactions, which provides good compositional control, is an alternative synthesis method which worth pursuing. The combustion synthesis enables synthesis at low temperatures and the products obtained are in a finely divided state with large surface areas. Furthermore, the nature of combustion synthesis is characterized by simple experimental set-up, short reaction time between the preparation of the reactants and the availability of the final product and less in external energy consumption (Aruna ,Mukasyan, 2008, Patil et al., 2002). Typically, the mixture of reactants consists of metal nitrate and a suitable organic fuel such as urea, glycine and citric acid. Additionally, the temperature is essential to boil the mixture until the ignition and self-sustaining reaction takes off. The large amount of gases formed can result in the appearance of a flame, which can reach temperatures in excess of 1000^{o}C. In some cases, the external source like simple calcination is necessary to accomplish the synthesis of the appropriate phase. This is because the energy released from the exothermic reaction between the nitrate and the fuel is usually ignited at a temperature much lower than the actual phase formation. Thus, the single phase formation is not ease to produce. Recently, our group had performed a modification on soft combustion synthesis, whereby nitrate salts, Bismuth (Bi) and organic Titanium (IV) isopropoxide (Ti) were dissolved into 2-methaoxyethanol and acetylacetone. In addition, the organic fuel was not used in this work. To introduce the doping content, the Sm^{3+} and Pr^{3+} from nitrate salts were also used. The observation of the soft combustion will be discussed in the following section.

5. Observation during the combustion process

Figure 1 shows the actual condition before and after combustion on BTO and Pr^{3+} doping. The Bi-Ti precursor was observed in clear-yellowish solution (**Figure 1a**) whereas the Pr^{3+} precursor was found in clear-greenish solution (**Figure 1b**). The Sm^{3+} precursor was observed in transparent solution (not shown here). The Bi-Ti precursor was then stirred at 40°C for 2 hours and the colour of the solution changed slightly milky-yellowish as shown in **Figure 1c**. The solution was then continuously evaporated and temperature maintained at ~90°C. The colour of the solution changed. It was found that higher Pr^{3+} doping tends to prolong hydrolysis process. After that, the temperature increased rapidly to ~120°C and the solution completely evaporated, resulting dark-yellowish gel (**Figure 1e**). The gel started to induced ignition at ~150°C. Metal nitrates were decomposed to form metal oxides and nitrogen. The compound was eventually acting as an oxidizer to continue the combustion synthesis, which was accompanied by the releasing of voluminous gases. At the end of this stage, flaming occurred and resulted foamy-like structure as shown in **Figure 1f**. The flaming temperature was found to be approximate 230°C. In order to remove the carbon

content in as-combusted powders, the calcination is necessary to enhance the degree of crystallinity with high purity of BTO content.

Fig. 1. Evolution of (a) Bi-Ti precursor (b) Pr precursor (c) Bi-Ti precursor stirred at 40°C for 2 hour (d) Bi-Ti precursor heated at 90°C (e) viscous gel and (f) as-combusted powder.

6. Powder characterization

6.1 Effect of calcination temperature on BTO

X-ray diffraction (XRD) was conducted on the as-combusted powders which calcined at different temperatures and the result is shown in **Figure 2**. The study on different calcination temperature is essential in this work. The main reason is to determine the optimum calcination temperature, which will be used for the following characterization in particular dielectric study. As seen in **Figure 2**, the BTO phase was observed in as-combusted powder. The main peak corresponding to BTO was found at ~29^{o}. However, the presence other intermediate phases such as BTO7.7 and BTO2 were also identified and marked in XRD pattern. At calcination temperature of 600^{o}C, there was a tremendous increase at the main peak (~29^{o}). This inedicates that the presence more BTO phase was observed after calcination process. In addition, the peaks corresponding to intermediate phases were decreased. Further increase calcination temperature, the intermediate phases were gradually eliminated. The intermediate phases completely disappeared at 750 and 800^{o}C. In other words, the BTO phase was successfully formed as single phase at temperature as low as 750^{o}C. It also suggest that the optimum calcination temperature for BTO is 750^{o}C. This temperature is probably lower than other processing route such as conventional solid state reaction and some other wet chemical synthesis (Kan et al., 2003, Pookmanee, 2008). Moreover, as the calcination temperature was increased, the XRD peaks were sharper and the stable phase BTO powders with higher crystallinity could be obtained. **Table 2** presents the variation of lattice parameters and

crystallite sizes of BTO calcined at different temperatures. As can be seen in **Table 2**, the corresponding lattice *a*-, *b*-, and *c*-parameters as well as volume cell units, V were observed to exhibit in various values as a result of calcination temperature. In addition, the crystal structure of calcined powder was confirmed to belong orthrhombic, in which it is a typical structure for BTO (Hervoches ,Lightfoot, 1999, Kim ,Jeon, 2004). Besides that, the crystallite size of calcined powder was increased with increasing calcination temperature. The increase in a such way was observed in many studies (Hou et al., 2010, Pookmanee ,Phanichphant, 2009, Umar Al-Amani et al., 2010).

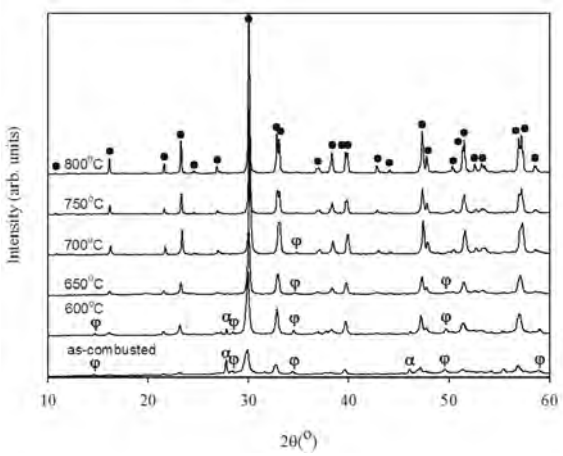

Fig. 2. XRD patterns of BTO powders calcined at different temperatures for 3 hour.
●:$Bi_4Ti_3O_{12}$ or BTO; α:$Bi_{7.7}Ti_{0.3}O_{12.16}$ or BTO7.7; φ:$Bi_2Ti_2O_7$ or BTO2.

Calcination, °C	600	650	700	750	800
a/ Å	5.418(2)	5.4138(6)	5.4110(6)	5.4093(2)	5.4066(2)
b/ Å	5.433(2)	5.4385(6)	5.4438(6)	5.4418(2)	5.4429(2)
c/ Å	32.765(6)	32.810(3)	32.853(4)	32.830(1)	32.817(1)
V/Å^3	964.4709	966.0297	967.7028	966.4148	965.7186
Crystallite Size/ nm	24.87	37.19	50.54	71.34	98.07

Table 2. Lattice parameters and crystallite sizes of BTO.

6.2 Effect of Sm^{3+} and Pr^{3+} doping on crystal structure and lattice parameter

The introduction of Sm^{3+} and Pr^{3+} to form $Bi_{4-x}Sm_xTi_3O_{12}$ (BSmT) and $Bi_{4-x}Pr_xTi_3O_{12}$ (BPrT) was expected to have a major changes on calcination temperature, crystal structure, lattice parameter and crystallite size. Based on previous studies, the ionic radii of Sm^{3+} and Pr^{3+} were reported around 0.108 nm and 0.113 nm, respectively, whereas the ionic radii of Bi^{3+} was about 0.117 nm (Garg et al., 2005, Hu et al., 2005). In general, the substitution of Sm^{3+} or Pr^{3+} for Bi^{3+} with larger difference in ionic radii size would lead to larger structure distortion of BTO lattice

(Hu et al., 2005). In addition, the increase in dopant contents would also result in difference in structure distortion (Kan et al., 2004, Kan et al., 2008). In order to determine the effect of Sm^{3+} and Pr^{3+} doping on crystal structure and lattice parameter, the calcined powder for respective contents were analyzed by XRD. Interestingly, the calcination temperature was successfully reduced from 750°C (for BTO) to 650°C (for BSmT and BPrT). According to **Figure 3**, the XRD patterns of BSmT and BPrT powders calcined at 650°C for 3 hour with different Sm^{3+} and Pr^{3+} contents were presented. Regardless of Sm^{3+} and Pr^{3+} contents, the formation of a single phase BTO was observed in **Figure 3(a)** and **Figure 3(b)** for both doping powders. This indicates that the perovskite phase was fully formed in calcined powders and all of them have a bismuth-layered structure. In comparison to the BTO calcined powder at 650°C for 3 hour (see **Figure 2**), the intermediate phases such as BTO2 and BTO7.7 were eliminated as a result of Sm^{3+} and Pr^{3+} doping. This result indicates that the Sm^{3+} and Pr^{3+} ions in the BSmT and BPrT, respectively, are incorporated into the pseudo-perovskite structure, substituting for the Bi^{3+} ions. Besides that, the lattice parameters and crystallite size of BSmT and BPrT were greatly influenced by Sm^{3+} and Pr^{3+} doping, as shown in **Table 3** and **Table 4**, respectively. Based on both tables, the *a*-parameter rapidly approached the *b*-parameter with increasing Sm^{3+} and Pr^{3+} content. The closed value of the *a*- and *b*-parameters was obtained at 1.0 mole of Sm^{3+} and Pr^{3+}, corresponding to the increment in the symmetry of the crystal structure. This also suggested that the orthorhombic structure was formed when doping content was equivalent to 0.25, 0.5 and 0.75 whereas the tetragonal structure was formed doping content was equivalent to 1.0. Further observation shows that the *c*-parameter slightly changed with increasing Sm^{3+} and Pr^{3+} content. It was reported that the variation of *c*-parameter is attributed to the rotation of the TiO_6 octahedron and the reduction in the oxygen deficient (Yoneda et al., 2006). It is evident that Sm^{3+} and Pr^{3+} had substituted in $(Bi_2Ti_3O_{10})^{2-}$ perovskite-type layers and O vacancies in the TiO_6 octahedron; these would eventually result in the shrinkage of unit cell. The crystallite size of BTO was found to be 37.19 nm and decreased continuously to 24.69 nm and 24.56 nm with 1.0 of Sm^{3+} and Pr^{3+}, respectively. It is attributed to the reduction of space charge density and oxygen vacancies with increasing Pr^{3+} content, which act as grain growth inhibiter. This is supported by the finding of Xiang et al. (Xiang et al., 2006). Based on XRD studies, it can conclude that the optimum calcination temperature for BTO was determined at 750°C, whereas the BSmT and BPrT were around 650°C.

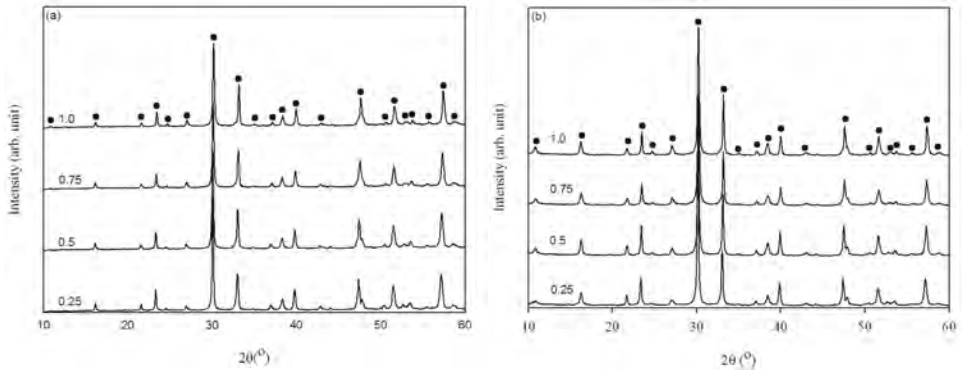

Fig. 3. XRD patterns of (a) BSmT and (b) BPrT powders calcined at 650°C for 3 hour with different Sm^{3+} and Pr^{3+} contents. ●:$Bi_4Ti_3O_{12}$ or BTO.

Sm^{3+} content	0.25	0.5	0.75	1.0
a/ Å	5.4076(3)	5.4018(4)	5.3952(5)	5.3910(1)
b/ Å	5.4283(3)	5.4155(4)	5.4059(5)	5.3940(1)
c/ Å	32.798(2)	32.803(2)	32.800(2)	32.777(2)
V/$Å^3$	962.74	959.6153	956.6382	953.0192
Crystallite size/nm	54.89	48.47	45.27	24.69

Table 3. Lattice parameters and crystallite sizes of BSmT.

Pr^{3+} content	0.25	0.5	0.75	1.0
a/ Å	5.4210(9)	5.4157(8)	5.4099(1)	5.4067(8)
b/ Å	5.4306(9)	5.4213(8)	5.4161(1)	5.4054(8)
c/ Å	32.783(3)	32.810(2)	32.816(3)	32.817(3)
V/$Å^3$	965.0938	963.3097	961.527	959.0734
Crystallite size/ nm	36.44	32.86	28.55	24.56

Table 4. Lattice parameters and crystallite sizes of BPrT.

6.3 Grain morphology of BSmT and BPrT powders

To gain an insight into the formation of BTO prepared using different doping content, the calcined powders were monitored by taking field emission scanning electron microscopy (FESEM) micrographs. **Figure 4** shows the morphology of BTO, BSmT and BPrT powders. In order to observe the increase in particle size of BTO, the morphology at 650°C and 750°C were displayed in **Figure 4a** and **Figure 4b**, respectively. It was found that the particle size is relatively expanded with increasing temperature. It was also determined that the particle size in range of 0.1 – 0.2 µm and 0.3 – 0.5 µm were found at 650°C and 750°C, respectively. It clearly observed that plate-like morphology was formed at 750°C instead of 650°C. The formation of such morphology was observed in many studies in which the plate-like structure with highly anisotropic properties is one of typical shape for pure BTO (Chen et al., 2006). In addition, the variation in particle size is also attributed to a greater distortion of perovskite-layer along *ab*-plane (particle length) as compared with *c*-axis (particle thickness). The morphology of BSmT and BPrT powders with different doping contents were observed and depicted in **Figure 4c – 4f**. In this section, the selected micrographs for each dopant with doping content of 0.25 and 1.0 were presented. The selection of the minimum and maximum doping contents is necessary to determine the variation size and shape of resultant particles. It was found that the particle size decreased with increasing doping content, corresponding to the lower diffusivity of both doping content compared to Bi^{3+}, resulting to the suppression of the grain growth (Goh et al., 2009). It was determined that the particle size in range of 0.2 – 0.4 µm and 0.1 – 0.2 µm were observed when Sm^{3+} contents were equivalent to 0.25 and 1.0, respectively. Meanwhile, the average particle size in range of 0.1 – 0.2 µm and 0.05 – 0.1 µm were found when Pr^{3+} contents were equivalent to 0.25 and 1.0, respectively. It is also noticed that the

size of plate-like particle decreased relatively with increasing Sm^{3+} and Pr^{3+}, corresponding to the greater relaxation in the perovskite-layer. In order to see the difference of the particle size between Sm^{3+} and Pr^{3+}, the doping content was fixed at 0.25. As can be seen in **Figure 4c** and **Figure 4e** for Sm^{3+} and Pr^{3+}, respectively, the particle size of Sm^{3+} doping was found to substantially larger than Pr^{3+} doping. This might be attributed to the difference in ionic radii which also resulted in different diffusivity.

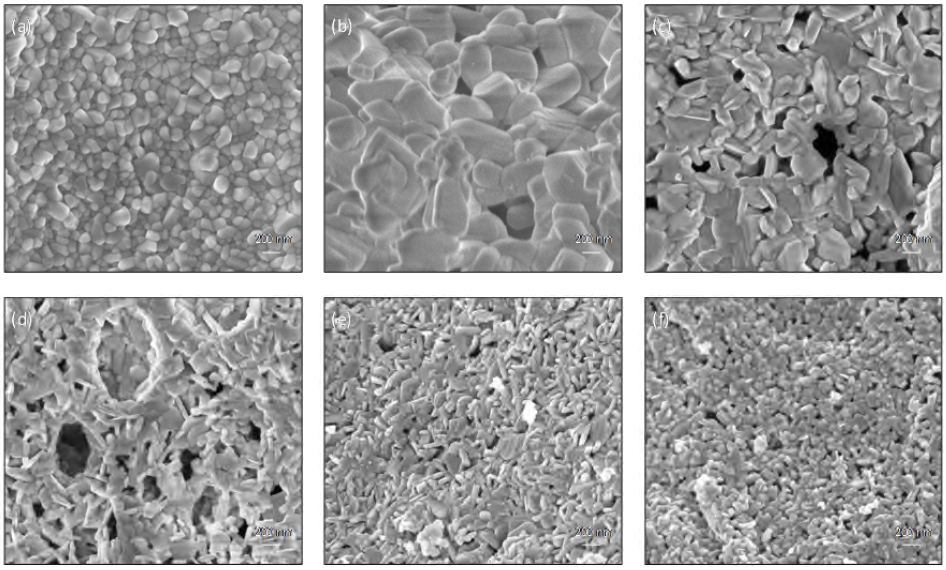

Fig. 4. Morphologies of (a) BTO:650°C, (b) BTO:750°C, (c) BSmT:0.25, (d) BSmT:1.0, (e) BPrT:0.25 and (f) BPrT:1.0.

6.4 Comparison of lattice vibration BTO and Sm^{3+} doping

In order to enhance the understanding of the doping effect from the structural point of view, Raman scattering study is a very useful tool for investigating the lattice vibrational modes, which can provide details of lattice vibrations changes. **Figure 5** shows the Raman spectra of BTO and BSmT powders at room temperature from 100 to 2000 cm^{-1}. Theoretically, the Raman selection rules allow 24 Raman active modes for orthorhombic BTO. (Kojima, 2000, Kojima ,Shimada, 1996). However, as shown in **Figure 5a**, the Raman spectrum of BTO less than 9 active modes were observed which is partially due to the possible overlap of the same symmetry vibrations or the weak features of some Raman bands (Liang et al., 2009). As can be seen in **Figure 5a**, the Raman modes at 193, 228, 267, 330, 353, 537, 563, 614 and 850 cm^{-1} were observed in BTO. All the Raman modes are also characterized as the vibrational modes of BTO which can be classified as internal modes of TiO_6 octahedra. According to Kojima et al. (Kojima ,Shimada, 1996), the internal modes of TiO_6 octahedra appear above 200 cm^{-1}. The mode at 850 cm^{-1} is attributed to the symmetric Ti – O stretching vibration of atom inside the TiO_6 octahedron whereas the mode at 614 cm^{-1} corresponds to the symmetry one. The two modes at 537 and 563 cm^{-1} correspond to the opposing excursions of the external apical oxygen (O) atoms of the $Ti0_6$ octahedron. The 228 and 267 cm^{-1} modes are ascribed to the O – Ti – O

bending vibration. Although the mode at 228 cm^{-1} is Raman inactive according to the *O*h symmetry of TiO_6, it is often observed because of the distortion of octahedron. The mode at 330 cm^{-1} was from a combination of the stretching and bending vibrations of the TiO_6 octahedron. In addition, the formation of BTO with orthorhombic structure is identified by the splitting mode at 193 and 228 cm^{-1}, and 537 and 563cm^{-1}. Nevertheless, the Raman modes of the lower wavenumber at 116 cm^{-1} was not found in this spectrum, to show the vibrations between Bi and O atoms. However, the reason of missing mode is still not clear. The effect of Sm^{3+} doping on the structure change of BTO on the basis of the Raman modes is presented in **Figure 5b**. It was clearly observed that the peak intensity decreased with increasing Sm^{3+} contents from 0.25 to 0.75. It is believed to be associated with strong interactions between the ionic bonds; corresponding to the smaller ionic radius of Sm^{3+} (0.108 nm) compared with Bi^{3+} (0.117 nm). With the increase of Sm content, the distortion structure would be more and the grain size would be smaller. This finding is in line with the XRD pattern and FESEM micrograph. It was reported that the duplet peaks observed in Raman spectra tend to merge into one mode when the Bi^{3+} is substituted by rare-earth elements (Wu et al., 2005). Similar observation was discovered in BST. In the present work, the duplet peaks at 228-267 cm^{-1}, 330-353 cm^{-1} and 537-563 cm^{-1} were found to merged into a single peak at 264 cm^{-1}, 322 cm^{-1} and 542 cm^{-1} for x= 0.25 and 264 cm^{-1}, 330 cm^{-1} and 553 cm^{-1} for x= 0.75.

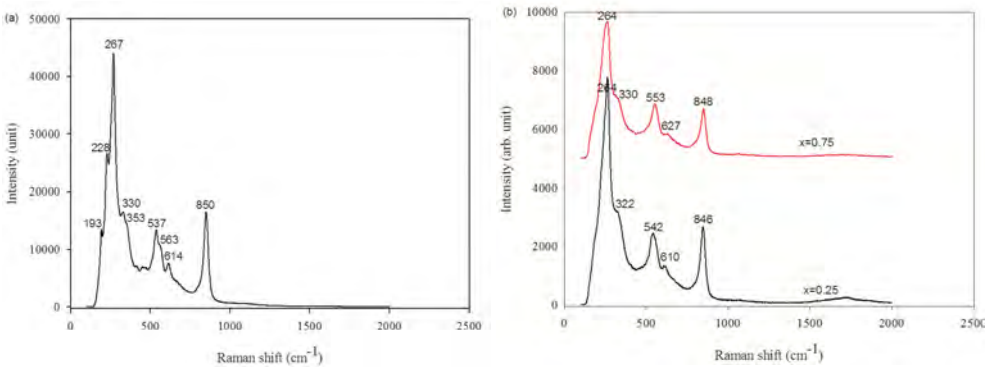

Fig. 5. Raman spectra of (a) BTO and (b) BSmT at different Sm^{3+} content.

7. Bulk ceramic characterization

7.1 Effect of sintering temperature of BTO

Figure 6 shows the XRD patterns of BTO ceramics sintered at different temperature for 3 hour. As can be seen from this figure, the BTO was formed with random oriented grains in which the strongest peak was found at (117) instead of (00l). Besides that, the increase in calcination temperature also implies the improvement of crystallinity and the enhancement of crystallite size. This can be explained by the width of the diffraction lines, which decreased, whilst the intensity increased. The crystallite sizes for ceramics sintered at 900, 1000 and 1100oC were calculated to be approximately 104.66, 126.52 and 130.22 nm, respectively.

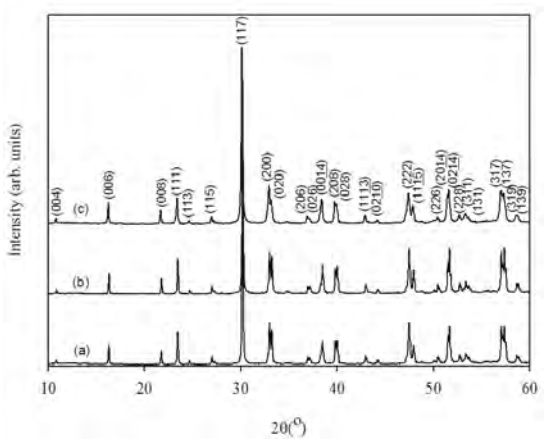

Fig. 6. XRD patterns of BTO ceramics sintered at different temperatures for 3 hour: (a) 900°C, (b) 1000°C and (c) 1100°C.

7.2 Effect of Sm^{3+} and Pr^{3+} doping on grain orientation

The preferred grain orientation was obviously affected by rare-earth doping in BTO particularly after sintering. Kannan et al. (Kannan et al., 2006) reported the reflections corresponding to (00*l*) plane along the *c*-axis was observed with increasing Nd^{3+} content from 0 to 0.25. It can give us another hint that preferred grain orientation would be different when rare-earth was introduced into BTO lattice. As discussed in **Figure 6**, the pure BTO was formed with no preferred grain orientation. In **Figure 7**, the XRD patterns of BST and BPT ceramics sintered at 1100°C for 3 hour were presented. As seen from this figure, the Sm^{3+} and Pr^{3+} doping show a highly *c*-axis oriented growth with increasing Sm^{3+} and Pr^{3+} contents. The XRD peak corresponding to (00*l*) plane was clearly observed with higher intensity as compared to (117) plane. To simplify the discussion, the peak at (00$\underline{14}$) and (117) are taken into consideration to determine the degree of *c*-axis orientation, α_c by Lotgering factor (Yang et al., 2008):

$$\alpha_c = I(00\underline{14})/[I(00\underline{14}) + I(117)]$$

The values of α_c calculated for the Sm^{3+} and Pr^{3+} doping with various contents are listed in **Table 5**. It was found that the degree of *c*-axis orientation increased with increasing Sm^{3+} and Pr^{3+} content. This indicates that the doping content has a significance result on grain orientation.

Sm^{3+} content	α_c (%)	Pr^{3+} content	α_c (%)
0.25	41.40	0.25	48.34
0.5	58.12	0.5	86.61
0.75	58.89	0.75	96.78
1.0	86.17	1.0	98.79

Table 5. Lotgering factor of the degree of *c*-axis orientation.

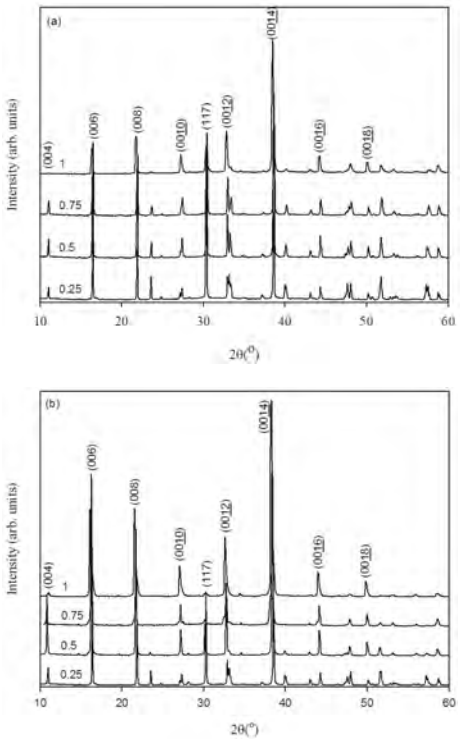

Fig. 7. XRD patterns of (a) BSmT and (b) BPrT ceramics sintered at 1100°C for 3 hour.

7.3 Microstructure of bulk ceramics after sintering

It is more interesting to observe the microstructure of bulk ceramics after sintering, as shown in **Figure 8**. Prior to view the micrograph using field emission scanning electron microscopy (FESEM), the surface of ceramics were polished on SiC papers grit 1000 followed by finer grit 2000. The polished ceramics were placed into ultrasonic for 10 minute to remove contaminants. The polished ceramics were thermally etched with temperature of 100°C lower than the sintering temperature for 30 minute. As can be seen in **Figure 8a**, the microstructure of the BTO ceramic shows a random arrangement of elongated-like grains, several of which are highly elongated. On the other hand, the microstructure of the BSmT and BPrT ceramics show a random arrangement of plate-like grains, as observed in **Figure 8b-8e**. It was also noticed that the average grain size relatively decrease with increasing Sm^{3+} and Pr^{3+} contents, indicating a strong influence of doping concentration which resulted in less amount of Bi^{3+} in BTO. The micrographs also revealed that the plate-like grains were not homogeneously distributed when Sm^{3+} and Pr^{3+} are equivalent to 0.25. Nevertheless, homogeneous microstructures with small grain size were found from the BSmT and BPrT ceramics with 1.0. The resultant micrographs was mainly attributed to a greater suppresion of the Bi^{3+} volatility by substitution of low diffusivity of Sm^{3+} and Pr^{3+}, which eventually inhibits the grain growth.

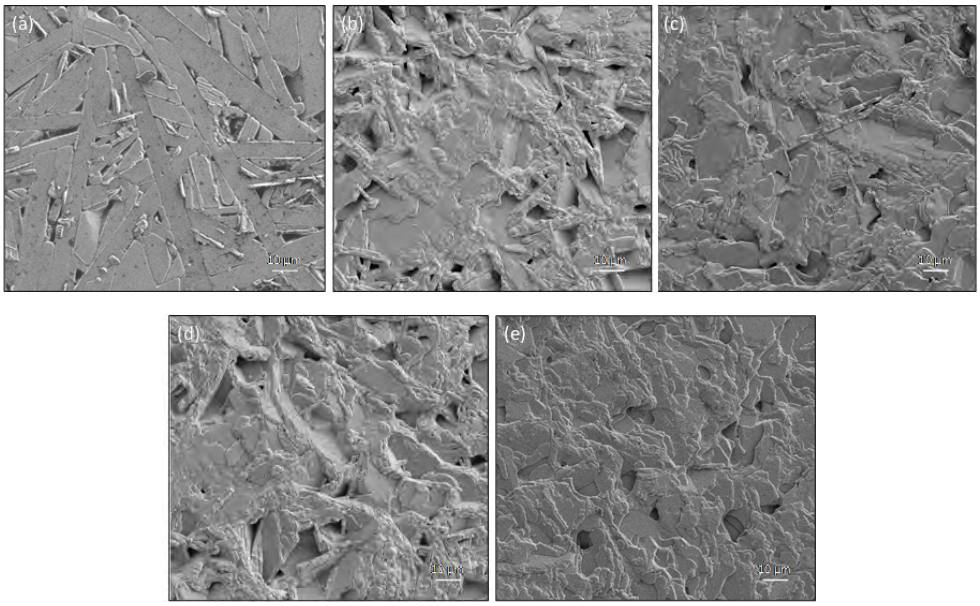

Fig. 8. FESEM micrograph of (a) BTO, (b) BSmT:025, (c) BSmT:1.0, (d) BPrT:025 and (e) BPrT:1.0, sintered at 1100°C for 3 hour.

7.4 Effect of sintering temperature and Sm^{3+}, Pr^{3+} content on relative density

The effect of sintering temperature on relative density of BTO ceramics was studied and depicted in **Figure 9a**. With increasing temperature, the relative density of ceramics was also increased up to 93% at 1100°C. This indicates that the densification behavior of BTO ceramics is temperature dependent. Thus, the sintering temperature at 1100°C was used for densification process with doping content. **Figure 9b** and **Figure 9c** show the relative density of Sm^{3+} and Pr^{3+} doping, respectively. As seen, the densities of BTO with doping content are different from one to another. It was determined that the densities was in range of 92 - 95%, indicating that a slight improvement as compared to pure BTO. The increase in relative density is associated to the decrease in Bi-loss during sintering resulting from the substitution effect by Sm^{3+} and Pr^{3+}. It can be said the small difference in relative density is another indicator to show the improvement of densification behavior in a such way.

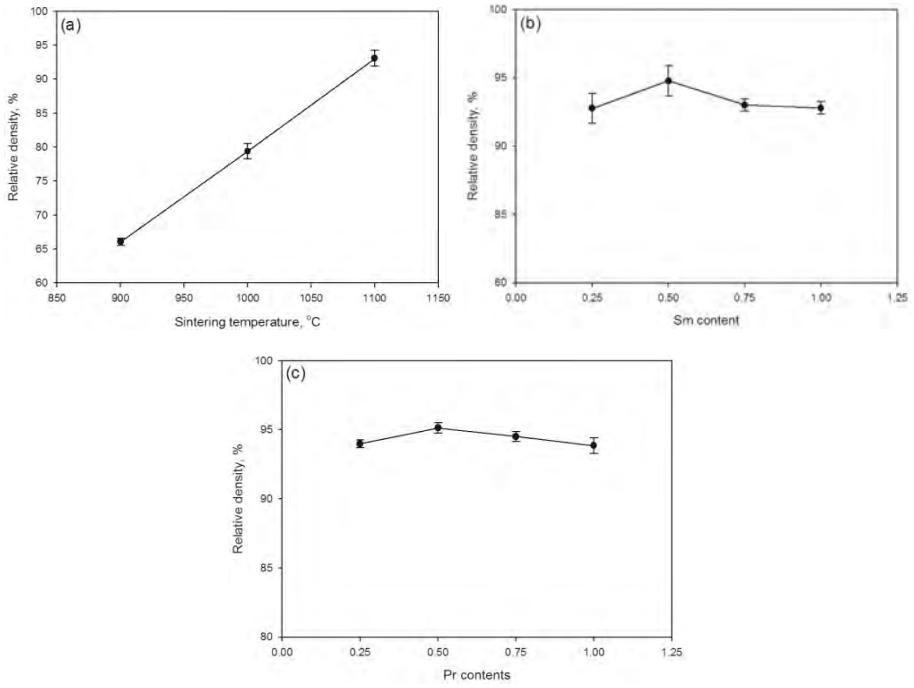

Fig. 9. Relative density of (a) BTO at different sintering temperatures, (b) BSmT with different Sm^{3+} contents and (c) BPrT with different Pr^{3+} contents; sintered at 1100°C.

7.5 Effect of Sm^{3+} and Pr^{3+} doping on dielectric properties

The effect of Sm^{3+} and Pr^{3+} contents in BSmT and BPrT on dielectric properties were studied. In this study, the measurement of dielectric constant, ε_r and dielectric loss, tan δ were performed at 1 kHz and at room temperature, 25°C and the results were presented in **Figure 10**. The variation of ε_r and tan δ were clearly observed in **Figure 10a** and **Figure 10b** for the BSmT and BPrT ceramics, respectively. The ε_r of the BSmT ceramics were in the range between 78 and 95, whereas the ε_r of the BPrT ceramics were in the range between 75 an 105. This indicates that the ε_r of the BPrT ceramics was slightly larger than the BSmT ceramics. This is associated to the larger ionic radii of Pr^{3+} than that of Sm^{3+}. This result can be explained by a shift of TiO^6 octahedra in a layered structure due to the substitution of larger ionic radii than that of Bi^{3+}. It was also noticed that the tan δ abruptly decreased with increasing Sm^{3+} and Pr^{3+} contents from 0.25 to 0.5. The decrement in the tan δ was attributed to a better electric flux caused by the reduction of grain imperfection. It was also supported by the increase in relative density, in which the ceramics appeared to be dense. Above 0.5, the tan δ were almost consistent with small difference in its value, corresponding to the reduction of the defects such as bismuth and oxygen vacancies. In order to see possible application as dielectric antenna, the dielectric study at different frequencies was performed. It was reported that the development of wireless technologies application requires very stringent criteria for dielectric ceramics materials. Typically, the dielectric ceramic materials must have a high dielectric constant, low dielectric loss and a a thermally

stable resonant frequency coefficient (LazareviÄ‡ et al., 2005). Thus, this study is essential to determine the potential application of such a field for the BTO, BSmT and BPrT ceramics.

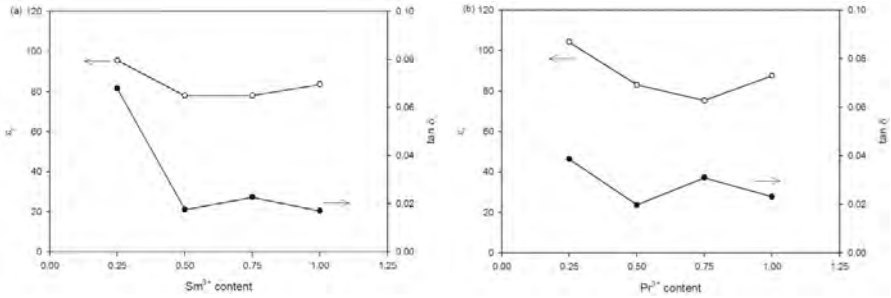

Fig. 10. Dielectric constant, ε_r and dielectric loss, tan δ at different doping contents: (a) BSmT and (b) BPrT.

7.6 Effect of various frequencies on the dielectric properties of the BTO, BSmT and BPrT ceramics

As reported in previous studies, the dielectric constant, ε_r and dielectric loss, tan δ were strongly dependent on frequency (Rachna et al., 2010, SimÃµes et al., 2008). In this work, the dielectric poperties were measured at different frequency ranges from 1 MHz to 1 GHz. As it can be seen from **Figure 11**, the ε_r of the BTO ceramic shows very obvious dispersion with

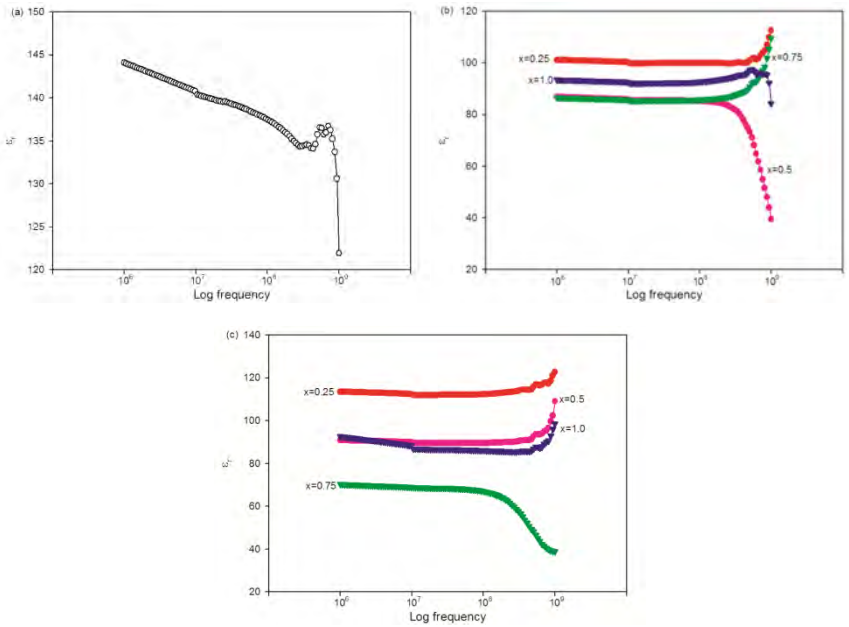

Fig. 11. Dielectric constant, ε_r of (a) BTO, (b) BSmT and (c) BPrT measured at high frequency range at room temperature.

frequency, indicating that the corresponding ceramic possess high defect concentration such as bismuth and oxygen vacancies. On the other hand, the ε_r of the BSmT and BPrT ceramics show very little dispersion from 1 MHz to 100 MHz. However, the ε_r shows very obvious dispersion above 100 MHz. This indicates the ε_r will be more complex at higher frequency range between 100 MHz and 1 GHz. The dielectric loss, tan δ at different frequencies was depicted in **Figure 12**. It was found that the tan δ of was slowly increased from 1 MHz to 10 MHz and abruptly increased from 10 MHz to 1 GHz, as shown in **Figure 12a**. In addition, the presence of relaxation peak in the tan δ was observed, as shown in inset **Figure 12a**. This indicates that the relaxation peak was observed approximately 700 MHz. It can be said that the increase trend in tan δ was also found in the BSmT and BPrT ceramics, as shown in **Figure 12b** and **Figure 12c**, respectively. Furthermore, the relaxation peaks in the tan δ was also observed around 700 MHz, which is almost comparable to BTO ceramic. The dielectric loss relaxation peak phenomenon can be explained by the Debye-like model for relaxation effects. The dielectric loss peak is maximal at the resonant frequency, which is the reciprocal of the relaxation time (Sulaiman et al., 2010). The dielectric loss relaxation may be generated by several possible factors such as surface roughness, distribution grain sizes and many more (Sulaiman et al., 2010, Wang et al., 2010). From the FESEM micrographs (see **Figure 8c to Figure 8e**) revealed that BSmT and BPrT with 1.0 have homogeneous distribution of grain sizes compared to 0.25.

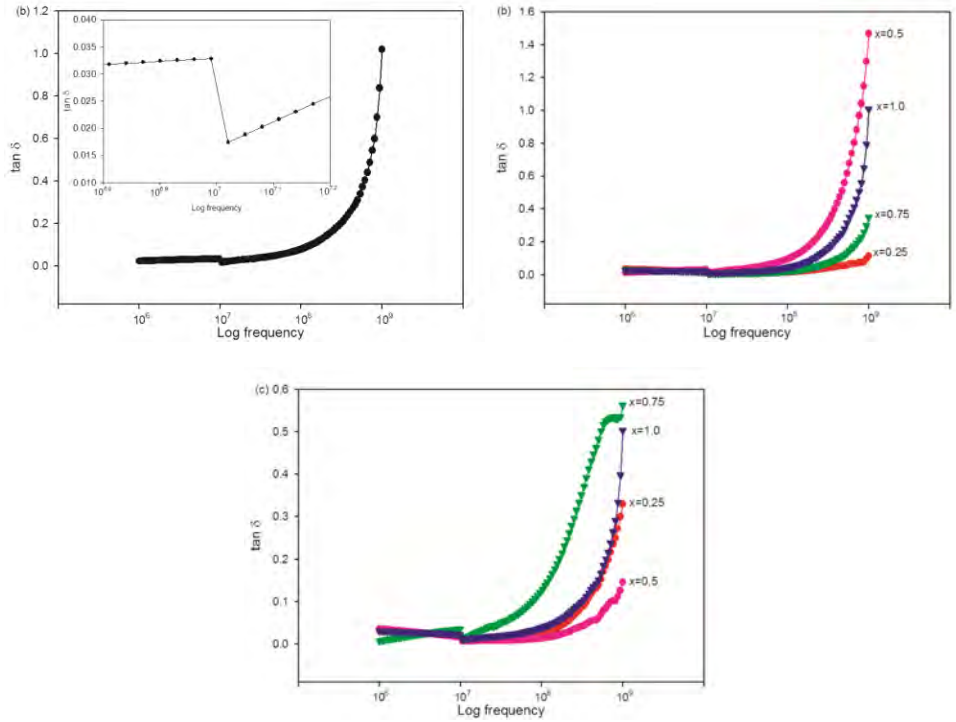

Fig. 12. Dielectric loss, tan δ of (a) BTO, inset showing the Debye relaxation effect, (b) BSmT and (c) BPrT measured at high frequency range at room temperature.

Therefore, the BSmT and BPrT with 1.0 gave a lower dielectric loss at relaxation frequency due to the above reason. Besides that, the improved ε_r with little dispersion and small variation in tan δ (or almost constant) can also suggest that the BSmT and BPrT ceramics are possible to be applied for wireless dielectric antenna applications instead of the BTO ceramic. However, a detail study is necessary to focus on return loss with a specific design of ceramic.

8. Conclusion

Based on this work, the rare-earth doping i.e. Sm^{3+} and Pr^{3+} had successfully improved the processing and properties of pure BTO ceramics. The calcination temperature was greatly reduced from 750°C to 650°C in order to form a single phase structure. The particle size of plate-like structure decreased continuously with increasing Sm^{3+} and Pr^{3+} content. The peak intensity and peak width in Raman spectrum were apparently low and broaden with increasing Sm^{3+} content. The Lotgering factor showed the enhancement in degree of *c*-axis orientation. The microstructure of the Sm^{3+} and Pr^{3+} doping showed a random arrangement of plate-like grains in which the grain size was relatively decrease at higher doping content. A great in densification behavior was also observed with Sm^{3+} and Pr^{3+} doping which resulted in the relative density of about 92-95% at 1100°C. The dielectric constant, ε_r of the BPrT ceramics was slightly larger than the BSmT ceramics, which can be explained in terms of larger ionic radii of Pr^{3+} than that of Sm^{3+}. The dielectric loss, tan δ of the BSmT and BPrT ceramics were greatly improved when dopant content above 0.5. For frequency study, the the ε_r of the BSmT and BPrT ceramics show very little dispersion from 1 MHz to 100 MHz instead of above 100 MHz. The relaxation peak in tan δ was observed approximately 700 MHz for all ceramics with different dopant contents. Based of frequency study, the BSmT and BPrT can be used as potential wireless dielectric antenna applications.

9. Acknowledgment

The authors appreciate the technical support from the School of Materials and Mineral Resources Engineering, Universiti Sains Malaysia. This research was supported by the USM Short term grant 6035276, USM-RU grant 1001/PBahan/8042018 and 811069.

10. References

Algueró, M., Ferrer, P., Vila, E., Iglesias, J. E. & Castro, A., Journal of the American Ceramic Society, 89 (2006) 3340.

Armstrong, R. A. & Newnham, R. E., Materials Research Bulletin, 7 (1972) 1025.

Aruna, S. T. & Mukasyan, A. S., Current Opinion in Solid State and Materials Science, 12 (2008) 44.

Besland, M. P., Djani-Ait Aissa, H., Barroy, P. R. J., Lafane, S., Tessier, P. Y., Angleraud, B., Richard-Plouet, M., Brohan, L. & Djouadi, M. A., Thin Solid Films, 495 (2006) 86.

Chen, W., Kinemuchi, Y., Watari, K., Tamura, T. & Miwa, K., Journal of the American Ceramic Society, 89 (2006) 490.

Cui, L. & Hu, Y. J., Physica B: Condensed Matter, 404 (2009) 150.
Du, X., Xu, Y., Ma, H., Wang, J. & Li, X., Journal of the American Ceramic Society, 90 (2007) 1382.
Du, X., Xu, Y., Ma, H., Wang, J. & Li, X., Journal of the American Ceramic Society, 91 (2008) 2079.
Garg, A., Hu, X. & Barber, Z. H., Ferroelectrics, 328 (2005) 93.
Goh, P. Y., Razak, K. A. & Sreekantan, S., Journal of Alloys and Compounds, 475 (2009) 758.
Golda, R. A., Marikani, A. & Padiyan, D. P., Ceramics International, (2011)
Guo, D. Y., Li, M. Y., Liu, J., Fu, L., Wang, J., Yu, B. F. & Yang, B., Materials Science and Engineering B: Solid-State Materials for Advanced Technology, 142 (2007) 135.
Han, K. & Ko, T., Journal of Alloys and Compounds, 473 (2009) 490.
Hardy, A., Mondelaers, D., Van Bael, M. K., Mullens, J., Van Poucke, L. C., Vanhoyland, G. & D'Haen, J., Journal of the European Ceramic Society, 24 (2004) 905.
Hervoches, C. H. & Lightfoot, P., Chemistry of Materials, 11 (1999) 3359.
Hou, J., Kumar, R., Qu, Y. & Krsmanovic, D., Journal of Nanoparticle Research, 12 (2010) 563.
Hu, X., Garg, A. & Barber, Z. H., Thin Solid Films, 484 (2005) 188.
Kan, Y. M., Zhang, G. J., Wang, P. L. & Cheng, Y. B., Journal of the European Ceramic Society, 28 (2008) 1641.
Kan, Y., Jin, X., Wang, P., Li, Y., Cheng, Y.-B. & Yan, D., Materials Research Bulletin, 38 (2003) 567.
Kan, Y., Jin, X., Zhang, G., Wang, P., Cheng, Y. B. & Yan, D., Journal of Materials Chemistry, 14 (2004) 3566.
Kan, Y., Wang, P., Li, Y., Cheng, Y. B. & Yan, D., Materials Letters, 56 (2002) 910.
Kannan, C. V., Cheng, Z. X., Kimura, H., Shimamura, K., Miyazaki, A. & Kitamura, K., Journal of Crystal Growth, 292 (2006) 485.
Ke, H., Wang, W., Chen, L., Xu, J., Jia, D., Lu, Z. & Zhou, Y., Journal of Sol-Gel Science and Technology, 53 (2010) 135.
Kim, J. S. & Kim, S. S., Applied Physics A: Materials Science and Processing, 81 (2005) 1427.
Kim, J. S., Integrated Ferroelectrics, 79 (2006) 139.
Kim, Y. I. & Jeon, M. K., Materials Letters, 58 (2004) 1889.
Kojima, S. & Shimada, S., Physica B: Condensed Matter, 219-220 (1996) 617.
Kojima, S., Ferroelectrics, 239 (2000) 55.
Kojima, T., Yoshida, I., Uekawa, N. & Kakegawa, K., Journal of the European Ceramic Society, 29 (2009) 431.
Kong, L. B., Ma, J., Zhu, W. & Tan, O. K., Materials Letters, 51 (2001) 108.
Lazarevic, Z. Stojanovic, B. D. & Varela J. A., Science of Sintering, 37 (2005) 199.
Liang, K., Qi, Y. & Lu, C., Journal of Raman Spectroscopy, 40 (2009) 2088.
Lu, C. J., Qiao, Y., Qi, Y. J., Chen, X. Q. & Zhu, J. S., Applied Physics Letters, 87 (2005) 1.
Macedo, Z. S., Ferrari, C. R. & Hernandes, A. C., Powder Technology, 139 (2004) 175.
Newnham, R. E., Wolfe, R. W. & Dorrian, J. F., Materials Research Bulletin, 6 (1971) 1029.
Ng, S. H., Xue, J. & Wang, J., Journal of the American Ceramic Society, 85 (2002) 2660.
Park, B. H., Kang, B. S., Bu, S. D., Noh, T. W., Lee, J. & Jo, W., Nature, 401 (1999) 682.
Patil, K. C., Aruna, S. T. & Mimani, T., Current Opinion in Solid State and Materials Science, 6 (2002) 507.

Pookmanee, P. & Phanichphant, S., Journal of Ceramic Processing Research, 10 (2009) 448.
Pookmanee, P., Journal of Ceramic Processing Research, 9 (2008) 30.
Pookmanee, P., Uriwilast, P. & Phanichpant, S., Ceramics International, 30 (2004) 1913.
Rachna, S., Bhattacharyya, S. & Gupta, S. M., Materials Science and Engineering B: Solid-State Materials for Advanced Technology, 175 (2010) 207.
Santos, V. B., M'Peko, J. C., Mir, M., Mastelaro, V. R. & Hernandes, A. C., Journal of the European Ceramic Society, 29 (2009) 751.
Shi, Y., Cao, C. & Feng, S., Materials Letters, 46 (2000) 270.
Simões, A. Z., Stojanovic, B. D., Ramirez, M. A., Cavalheiro, A. A., Longo, E. & Varela, J. A., Ceramics International, 34 (2008) 257.
Stojanovic, B. D., Paiva-Santos, C. O., Cilense, M., Jovalekic, C. & Lazarevic, Z. Z., Materials Research Bulletin, 43 (2008) 1743.
Stojanovic, B. D., Paiva-Santos, C. O., Jovalekic, C., Simoes, A. Z., Filho, F. M., Lazarevic, Z. & Varela, J. A., Materials Chemistry and Physics, 96 (2006) 471.
Stojanovic, B. D., Simoes, A. Z., Paiva-Santos, C. O., Quinelato, C., Longo, E. & Varela, J. A., Ceramics International, 32 (2006) 707.
Subbarao, E. C., Journal of Physics and Chemistry of Solids, 23 (1962) 665.
Subbarao, E. C., Physical Review, 122 (1961) 804.
Sulaiman, M. A., Hutagalung, S. D., Ain, M. F. & Ahmad, Z. A., Journal of Alloys and Compounds, 493 (2010) 486.
Thongtem, T. & Thongtem, S., Ceramics International, 30 (2004) 1463.
Umar Al-Amani, A., Srimala, S., Ahmad Fauzi, M. N. & Khairunisak, A. R., Malaysian Journal of Microscopy, 6 (2010) 69.
Wang, C. M., Lin, S. Y., Kao, K. S., Chen, Y. C. & Weng, S. C., Journal of Alloys and Compounds, 491 (2010) 423.
Wang, X. S., Zhang, Y. J., Zhang, L. Y. & Yao, X., Applied Physics A: Materials Science and Processing, 68 (1999) 547.
Watcharapasorn, A., Siriprapa P. & Jiansirisomboon S., Journal of the European Ceramic Society, 30 (2010) 87.
Wu, D., Deng, Y., Mak, C. L., Wong, K. H., Li A. D., Zhang M. S. & Ming N. B., Applied Physics A: Materials Science and Processing, 80 (2005) 607.
Xiang, P. H., Kinemuchi, Y. & Watari, K., Materials Letters, 60 (2006) 2837.
Xie, L., Ma, J., Wu, P., Tian, H., Zhao, Z., Zhou, J., Hu, Y., Wang, Y., Tao, J. & Zhu, X., Materials Research Bulletin, 42 (2007) 389.
Xue, K. H., Celinska, J. & Paz De Araujo, C. A., Applied Physics Letters, 95 (2009)
Yan, H., Zhang, H., Zhang, Z., Ubic, R. & Reece, M. J., Journal of the European Ceramic Society, 26 (2006) 2785.
Yan, N. C. & Razak, K. A., Journal of Alloys and Compounds, 509 (2011) 942–947
Yang, B., Zhang, D. M., Zhou, B., Huang, L. H., Zheng, C. D., Wu, Y. Y., Guo, D. Y. & Yu, J., Journal of Crystal Growth, 310 (2008) 4511.
Yang, Q., Li, Y., Yin, Q., Wang, P. & Cheng, Y. B., Journal of the European Ceramic Society, 23 (2003) 161.
Yoneda, Y., Kohara, S. & Mizuki, J., Japanese Journal of Applied Physics, Part 1: Regular Papers and Short Notes and Review Papers, 45 (2006) 7556.

Zdujić, M., Jovalekić, Č., Poleti, D., Veljković, I. & Karanović, L., Journal of Non-Crystalline Solids, 352 (2006) 3058.

Zhi-hui, C., Jun-fu, Q., Cheng, L., Jian-ning, D. & Yuan-yuan, Z., Ceramics International, 36 (2010) 241.